A Calibration Study of the ANITA Instrument

A Senior Honors Thesis

Presented in Partial Fulfillment of the Requirements for Graduation *with research distinction* in Physics in the undergraduate colleges of The Ohio State University

by

Christopher Williams

The Ohio State University

May 2008

Project Advisor: Professor James Beatty, Department of Physics

Abstract

The Antarctic Impulsive Transient Antenna (ANITA) is a balloon-borne experiment that flew for 35 days in the 2006/07 austral summer looking for ultra-high energy neutrinos (10^{18}-10^{20}eV) interacting within the Antarctic ice. These ultra-high energy neutrinos are believed to be produced primarily through cosmic ray attenuation by the Cosmic Microwave Background (CMB) via the Greisen-Zatsepin-Kuzmin (GZK) mechanism. This research serves as a study of the observed radio background over the 1GHz (200MHz-1.2GHz) band that ANITA was sensitive to. We look for significant anthropogenic noise anomalies as well as confirmation of a thermal noise background. Radio noise from the sun and galactic center is also observed and confirmed to match predicted values. Analysis of the sun/galactic center radio noise was done using pointing software based on the payload's spatial location given by onboard GPS. We also study the synchronization of the on-board calibration pulsing antennas with the instrument's triggering system. This is necessary to confirm that events observed by hardware triggering have correctly matching information provided by software.

1 Introduction

Griesen, Zatsepin, and Kuzmin simultaneously predicted a fall-off in the cosmic ray spectrum for ultra-high energy (UHE) cosmic rays in 1966. It was predicted that UHE cosmic rays produced beyond 40 Mpc will be attenuated by the cosmic microwave background (CMB)[1, 2]. At energies above 10^{20} eV, the incoming cosmic ray primary has large enough energy to undergo photo-pion production with the CMB via the Δ^+ resonance.

$$\begin{aligned} p + \gamma_{CMB} \rightarrow \Delta^+ &\rightarrow \pi^0 + p \quad (1) \\ &\rightarrow \pi^+ + n \quad (2) \end{aligned}$$

The predicted drop in UHE cosmic ray flux has been observed by both the Hi-Res collaboration and the Auger collaboration on their respective experiments [4, 5]. It can not be said definitively whether the observed drop in flux is due to the GZK cut-off or a source effect. The decay of the π^+ in equation (2),

$$\pi^+ \rightarrow \mu^+ + \nu_\mu \tag{3}$$

$$\mu^+ \rightarrow e^+ + \nu_e + \overline{\nu}_\mu \tag{4}$$

will result in UHE neutrinos with an energy range of 10^{18}-10^{20} eV shown in Equations (3) and (4). If observed these neutrinos will be a signature of the GZK effect, independent of the cut-off in the cosmic ray spectrum.

The GZK effect is thought to be the most likely source of UHE neutrinos. Other, direct, sources may include gamma-ray bursts and active galactic nuclei, but their ability to produce UHE neutrinos is currently unknown. More exotic sources include topological defects and z-burst neutrinos [3].

In 1962, Gurgen Askaryan showed that excess negative charge in an electron-photon shower will develop and produce Cherenkov radiation [6]. Askaryan also showed that the Cherenkov pulse will be coherent for wavelengths larger than the dimensions of the shower front and the corresponding pulse intensity will be proportional to square of the shower energy. Because the dimensions of the shower are determined by the medium in which the shower is traveling Askaryan suggested using a dense detection medium such as lunar regolith. This would have the effect of creating a coherent radio pulse with wavelength of order 10 cm. This corresponds to a frequency of 3 GHz which is a very practical band of the electromagnetic spectrum to make large scale measurements in.

2 Antarctic Impulsive Transient Antenna

A more practical terrestrial medium to work in is ice. Gorham et. al. confirmed the Askaryan effect in ice with the Antarctic Impulsive Transient Antenna (ANITA) in 2006 using the Stanford Linear Accelerator and a 7.5 tonne ice block as a beam target. The Askaryan signal was confirmed in the 200-1200 MHz band in which ANITA is sensitive. The received power was also shown to scale as the square of the shower energy as predicted [7].

Ice, like lunar regolith, is a dense medium which is necessary to keep particle shower dimensions small, concentrating the coherent pulse into a useable frequency band. Ice is also nearly transparent to radio signals. Barwick, et. al. show the attenuation length for a 380 MHz radio signal to be 1450^{+300}_{-150}m [8]. With regards to the ANITA experiment the Antarctic ice sheet is an ideal medium because it provides an enormous detection volume with relatively low radio noise which is necessary to deal with the low flux of high

energy neutrinos. Also, with an attenuation length of roughly 1.5 km nearly all radio pulses from transient interactions will escape the ice sheet.

The ANITA instrument is an antenna array consisting of 32 quad-ridged feed horns. These feed horns are divided up into 16 phi sectors which contain a lower and upper ring antenna. The instrument's engineering schematic is shown in Fig. 1 with adjacent phi sectors highlighted in red and blue. The 32 feed horns are dual-polarized, having a channel for both vertical and horizontal polarization.

Not pictured in Fig. 1 are 4 discone and 4 bicone antennas that were mounted on the payload frame above the lower ring of antennas. The 4 bicone antennas were also used as calibration pulsing antennas that are discussed in §4.3 of this paper.

The read-out electronics log a number of parameters, most important to this analysis are GPS location and timing, a measurement of relative power for each channel, and trigger timing. Header flags describing the timing and status of the instrument are also used in this analysis, as well as waveforms on all 64 channels.

2.1 Flight

For flight ANITA takes advantage of the NASA Columbia Science Balloon Facility (CSBF) base at McMurdo, Antarctica. The payload is attached to a long duration balloon and released into the polar vortex, an annual weather pattern centered on the south pole. Once in the polar vortex the payload sits aloft at approximately 37 km above the Antarctic surface. This gives the payload an effective horizon of 600 km. With this horizon ANITA has an effective observing volume of 2.26×10^6 km^3. This large volume is necessary for two reasons. UHE neutrinos have a mean free path of order 400 km in ice and the expected flux of UHE neutrinos is expected to be low. Due to geometric constraints ANITA is only sensitive to horizontally transient interactions as seen in Fig. 2. Down-going events are unlikely to interact in the $\sim$2 km depth of ice before bedrock and would not give the correct angles to produce an upward moving Askaryan pulse. Up-going neutrinos will interact in the earth screening all UHE neutrinos from the northern hemisphere. With these constraints Barwick et. al. predict through simulation that ANITA would observe 5-50 events over a 50 day flight [3].

This prediction was made for a standard flight path which usually places balloons into an approximate latitude of 80^o S. As shown in Fig. 3, the

2006/07 polar vortex did not lock into place over the South Pole as usual. This forced ANITA's path over both shallower, warmer ice and near more anthropogenic noise sources. Because the ANITA flight path was non-standard the number of observed events is expected to be lower and understanding the RF background and instrument calibration is very important.

2.2 GPS pointing

Because the ANITA instrument is an array of multiple antennas viewing 2π steradians, pointing can be done using interferometry based on the arrival time of signals. This is time consuming because reconstruction is necessary for each individually triggered event. In order to have a pointing solution that can be accessed quickly and used for low trigger level events a software suite was developed to do coordinate conversion in multiple frames.

The coordinate conversion software uses the six axis GPS position of the instrument given by an ADU5 GPS unit. The ADU5 unit gives standard aeronautical parameters: latitude, longitude, altitude, heading, pitch and roll. Conversions are made to know the location of the payload relative to the center of the earth. Using this geocentric frame, transforms can be done for any terrestrial object assigning coordinates in a Cartesian frame based on the payload's location with the origin centered at the payload. Similarly, astronomical objects can be given coordinates of altitude and azimuth (alt/az) relative to the payload. The sun's position relative to the payload is also stored for all times in payload alt/az coordinates. This value is calculated from standard UNIX allowing for conversions for all dates after Jan. 1, 1970. The phi sector that the object occupies is also stored, which proved useful for RF background analysis.

The coordinate suite can transform to any of the above frames from the following initial coordinates: WGS84 Cartesian coordinates; Latitude, Longitude, and Altitude; RA and Dec; Galactic Latitude and Longitude; and payload alt/az. Because the pointing accuracy of the coordinate suite is limited to the error in GPS measurements ($\sim 1^{\circ}$) interferometry will always be the primary pointing method for event reconstruction. This software simply serves as a first order check on analysis and a way to handle pointing for a large number events, or known objects.

3 RF Power Analysis

The initial analysis of the radio frequency (RF) background was to examine the total average instrument power in time. This was followed by an analysis of power averaged over each phi sector to confirm that sun and galactic center added the expected thermal component. The final piece of the RF background analysis looks at the South Pole as an anthropogenic noise source.

For this paper all RF power measurements are presented in Analog to Digital Converter (ADC) counts. This is done because absolute power calibration for the instrument is still pending. All of this analysis is concerned only with pointing and background response due to anthropogenic noise and astronomical sources so relative measurements are sufficient.

3.1 RF Background

Fig. 4 shows the power for the instrument read from the sampling board and averaged over 32 channels of a single polarization, with the top panel corresponding to horizontal polarization and the bottom panel vertical polarization. There is a significant amount of anthropogenic noise when in view of bases. These areas are marked on the graph by red arrows. The Sinusoidal variation is due to the diurnal period, with thermal noise from the sun/galactic center increasing as their altitude decreases. The amplitude of the diurnal variation is largely dependent on latitude. The single noise increase in the quiet period on December 30 (Marker 3) occurs when the payload moves out over the ocean and the thermal noise floor rises due to warm water being within the instruments horizon. The flight path over the ocean is shown in the red path in Fig. 3.

The observed background is what was expected of the thermal background in time. The diurnal period is seen and the increased background relative to the noise floor when near bases is observed as expected. The radio noise is much stronger in the vertical polarization than the horizontal, which is expected of anthropogenic signals seen at 1 and 2 on Fig. 4.

3.2 Solar and Galactic Center Components

To test the solar/galactic center components of the noise background the coordinate suite was used to isolate the phi sector that contained the sun. The average power for each phi sector is then plotted with the sun centered

at 0 in Fig. 6. Positive phi sectors correspond to moving right around the instrument, while negative phi sectors correspond to moving left. Because each antenna has a beam size of roughly 45° it is impossible to separate the sun from the galactic center even at the end of the flight. The separation relative to ANITA's frame is plotted in Fig. 5 for the length of the flight.

Because it is impossible to spatially separate the sun and galactic center the simplest interpretation would be to expect an excess in the direction of the sun with a symmetric decline in power on both sides. Fig. 6 shows the average power for each phi sector when the South Pole is in view of the payload. While the local maximum occurring at the sun is seen, and the decline seems relatively symmetric, the average power values are not distributed evenly. This can be attributed to anthropogenic noise and other triggered noise spreading the distributed averages for certain phi sectors at a given time. This is also the cause of the large range of background values seen in purple in Fig. 6.

3.3 Anthropogenic Noise Effects

Anthropogenic noise has a strong effect in the vertical polarization. This is clearly seen in Fig. 4 when the payload is near bases. On the second pass by the South Pole base there is almost no noise seen in the horizontal polarization, while the base is fully visible in the vertical. This can not be used to our advantage in neutrino detection because ANITA is much more likely to detect the vertically polarized component of the Askaryan pulse because the payload would most likely be near the top of the Cherenkov cone for a given event.

It is possible to isolate the anthropogenic noise spatially. Fig. 7 contains the same data as Fig. 6 plotted for a different geometry with the South Pole at zero and the corresponding phi sectors to the left and right of the base. In Fig. 7, when the South Pole is centered and the average power per phi sector is plotted the effect the base has on the noise background is clearly shown. This suggests that masking off phi sectors when they are in view of a base may help establish a thermal noise floor for the instrument making triggering more efficient. A masking of the 7 phi sectors centered on the South Pole is shown in Fig. 8. Masking these phi sectors completely eliminates the noise component from the South Pole. The color scale in Fig. 8 displaying number of events is held fixed, this is done to maintain consistent number resolution in each bin. The power distribution has had many events removed,

lowering the maximum number per bin. Beyond this fact, the average power distribution now shows a much smoother distribution between phi sector, and a nearly constant green band is now seen showing the thermal noise floor.

4 Calibration Pulser Study

In flight it was noticed that the triggering had a trigger timing bit slip on some events. This suggests that the software header information was not correctly matched to the other data being recorded by the instrument. The software header contains information for each event including: GPS timing, nanosecond timing within the GPS second, and various status flags.

The onboard calibration pulser is an excellent way to study this timing mismatch because it pulses with a known waveform at a rate of 1Hz on the GPS second. Therefore, it should be easy to find pulsing events in the data based on waveform analysis.

The following analysis deals with the two quiet periods in the flight when the instrument was stable (Dec. 18, 2006 to Dec. 22, 2006 and Dec. 27, 2006 to Jan. 4, 2007). These dates can be seen in Fig. 4 as being at the thermal noise floor away from major bases.

4.1 Calpulser Anatomy

The onboard calibration pulser used the four bicone antennas attached to the payload frame above the lower ring. The antennas were pulsed periodically throughout the flight using an Avtech pulser with eight attenuation settings attached to a 4 port switch connecting it to each antenna. The pulser was set up to pulse at a 1Hz rate every one to six hours depending on software settings. During this pulsing series the pulser should have produced one pulse for each attenuation on each of the 4 antennas, 32 pulses total. A header flag, calibStatus, consisting of a 2 byte bit mask contained information about pulsing. This information includes when pulsing was on, which antenna is pulsing, and what the attenuation setting was. During a pulsing session the calibStatus bit mask is set for the entire duration of the second.

4.2 Missing Pulses

To initially look for any sync slips header information was plotted in time. This was meant to be a first order check to ensure the pulser was working properly, before doing any waveform analysis. Plotting the pulsing sequences from the header information revealed that the pulser had not been working properly. Approximately one third of the expected 32 pulses in a sequence had been recorded. Further investigation showed that the received pulses appeared to come in randomly, not following the repeated pattern in attenuation pulsing order provided by software.

This problem was confirmed to be a hardware malfunction by testing the pulser from the recovered payload. The pulser did pulse sporadically without the expected order in attenuation. Had this hardware malfunction not been the case it would have been possible to know the number of expected pulses, identify those that were missing, and attempt to locate them within the data set. With this malfunction that analysis was impossible, but the waveform analysis still proved useful in looking for missing pulses and mislabeled pulses. Fortunately, the pulser did change pulsing antenna order with a regular pattern throughout the flight. This periodicity proved valuable in the waveform analysis of the calibration pulses.

4.3 Timing Sync Mismatch

A mislabeled calibration pulse is a clear indicator of a timing sync slip and is the major motivation for the waveform analysis because triggering bit slips for other events were observed in flight. Another possible scenario is pulses being far from the GPS second due to hardware malfunction and consequently would not be labeled as a calibration pulse. This type of timing mismatch was also seen in flight. In this case far from the GPS second is considered as being greater than 200 ns from the second. This is chosen because it is a clear break in the timing for all events labeled as calibration pulses. This is an arbitrary cut that is necessary because the calibStatus flag is on for the full second allowing other triggered events to have the same header information as the calibration pulser. This cut would have been easily tunable if it excluded many real pulses.

In order to find any mislabeled pulses as well as labeled pulses far from the GPS second a search of the events was made independent of header information. To accomplish this a method of identifying pulses by their

waveforms was developed.

4.3.1 Cross-Correlation Analysis

A cross-correlation analysis was used to with a template waveform. The template waveform was a lowest attenuation calibration pulse on pulsing antenna 1. The template consists of 64 individual waveforms from each of the instrument's channels. The cross-correlation, described in Equation (5), translates two functions through one another in time. The result is a secondary function that shows strength of correlation from the peak value of the function and timing variation as an offset from zero. This offset is used to describe trigger timing.

$$f \star g \equiv \int_{-\infty}^{\infty} f^*(\tau) g(t+\tau) d\tau \tag{5}$$

A cross-correlation of a waveform with itself, an auto-correlation, is the model of an ideal correlation. The middle panel of Fig. 9 shows an auto-correlation from one channel in the template waveform. An auto-correlation will have the maximum possible peak value, it will be positive, and centered at zero time. It will also be symmetric about the origin because the auto-correlation has no trigger time offset.

A list of 313 labeled pulsing events for pulsing antenna 1 were chosen as a test sample. This list of events was populated only from the calibStatus mask and requiring that event trigger time was within 200 ns of the GPS second; waveforms were not looked at in making this list. Using the template event a cross-correlation was done for all of the events correlating each of the 64 channels with its corresponding partner in the template. With this analysis cuts were chosen to exclude the 10 pulses that were labeled but had no pulse. The labeled events with no pulses were identified from the waveforms and are expected to be a consequence of the pulsing hardware malfunction.

The cuts used are shown in Table 1. It was identified that for pulsing antenna 1 the maximum correlation value always occurred in the vertical polarization of instrument on antenna 14 (Ant14 vPol). This is what is expected based on the geometry of the instrument. The most robust cut in identifying pulsed waveforms was found to be taking a Hilbert envelope over the top of the correlation. This assigns an analytic function to the waveform. This Hilbert envelope was then normalized and fitted with a Gaussian. The width of the Gaussian was then used as a descriptor of correlation. Fig. 10

shows a good correlation. The middle panel is the correlation for Ant14 vPol and the bottom panel shows the normalized Hilbert Envelope fitted with a Gaussian. Fig. 11 is composed of the same graphs for a bad correlation. The difference between these figures in very clear. The good correlation has a stronger maximum value, and a normalized Hilbert Envelope with a much smaller width.

After these cuts were tuned to find all of the known pulses a cross-correlation using the template was performed on a set of 1600 events that included only 4 pulsed events. This was done to test the robustness of the cuts and allow for additional fine tuning. Once the cuts found only the 4 real pulses in the data set of 1600 events the cross-correlation analysis was performed for all of the events in the two quiet periods outlined above.

4.3.2 Results

The result of the cross-correlation analysis is shown in Fig. 12 plotted as pulsing antenna number from header information as a function of time. The gray markers indicate header labels of pulses on all pulsing antennas with the gray line showing time ordering. The blue triangles are the pulses that are found by the analysis plotted with their original header information. Because this analysis is only looking at pulsing antenna 1 all of the blue triangles should be on antenna 1. The found pulses on antennas 2 and 4 show a mislabeling. There is a marker for every pulse, but because this graph shows a long length of time the markers for all of the different attenuation settings overlap. This is inconsequential and the markers can be thought of as packets of pulses.

The found pulses labeled as antenna 4 are composed of three events that passed the cuts but are not pulses on antenna 1. There are also six events found as pulses that have a bad calibStatus bit mask. These are denoted in Fig. 12 with pulsing antenna value -1. These are are real pulses that would be matched correctly if the calibStatus flag was correct.

Eight events are found to be pulsed events on antenna 1 but have a trigger time greater than 200 ns from the GPS second. These events are denoted by either black circles or squares in Fig. 12. Squares correspond to events that are not labeled as pulsing antenna 1. Circles correspond to events properly labeled as pulsing antenna 1. These properly labeled events can be tracked back to header labeled events that have no pulse in a number of cases. The eleven header labeled events with no pulse are denoted by red circles.

Most interesting is the number of found pulses occurring with antenna label 2. They don't occur regularly, but they are very systemic when they do occur. The events always align in time with the switch from pulsing antenna 2 to pulsing antenna 1. This is a clear indication of a timing sync slip for the calibStatus flag in the header. It may also indicate a timing sync slip with the header information in general, with the pulsing antenna ahead of the header information.

5 Conclusion

This study showed no significant noise anomalies above thermal background for the first flight of the ANITA instrument. The sun and galactic center behaved as expected with their contribution largely dependent on direction. Anthropogenic noise also behaved as expected being largely concentrated in the vertical polarization. Using phi sector masking this noise can be reduced significantly when near major bases returning the instrument to a thermal noise background at the cost of not triggering on a number of the instrument's phi sectors.

This study also showed a mismatch in header information for the calibration pulser. It is inferred that this mismatch is a slip in timing synchronization beyond the discovered hardware malfunction of the pulser. At best this is only a mismatch in the calibStatus flag. It is possible, however, that timing is off for waveforms as well. This implies that header timing information for the waveforms is not a robust measurement at the level of seconds and should be used cautiously in waveform analysis. This should have little effect on any signal analysis for the instrument since this is primarily done through interferometry using the nanosecond timing of waveforms. It will be useful, however, to identify mislabeled calibration pulser events so they are not reconstructed as signal.

References

[1] K. Greisen: 1966 Phys. Rev. Lett. **16**, 748

[2] G. T. Zatsepin and V. A. Kuzmin: 1966 J. Exp. Theor. Phys. Lett. **4**, 78 [1966 ZhETF Pis'ma, 4, 114-117]

[3] S. Barwick et. al.: 2006, Phys. Rev. Lett. **96** 171101

[4] Hi-Res Collaboration: 2008, Phys. Rev. Lett. **100**, 101101

[5] T. Yamamoto for the Pierre Auger Collaboration: 2007, Proceedings from the 30th International Cosmic Ray Conference

[6] G. A. Askaryan: 1962. Sov. Phys. JETP, 14, 441

[7] P. W. Gorham et. al. [The ANITA Collaboration]: 2007 arXiv:hep-ex/0611008v2

[8] S. Barwick et. al.: 2005. Journal of Glaciology, Vol. 51, No. 173, 231

[9] M. Rosen for the ANITA Collaboration: 2006 ANITA Schematic

[10] R. Nichol for the ANITA Collaboration: 2007 Flight Path Map

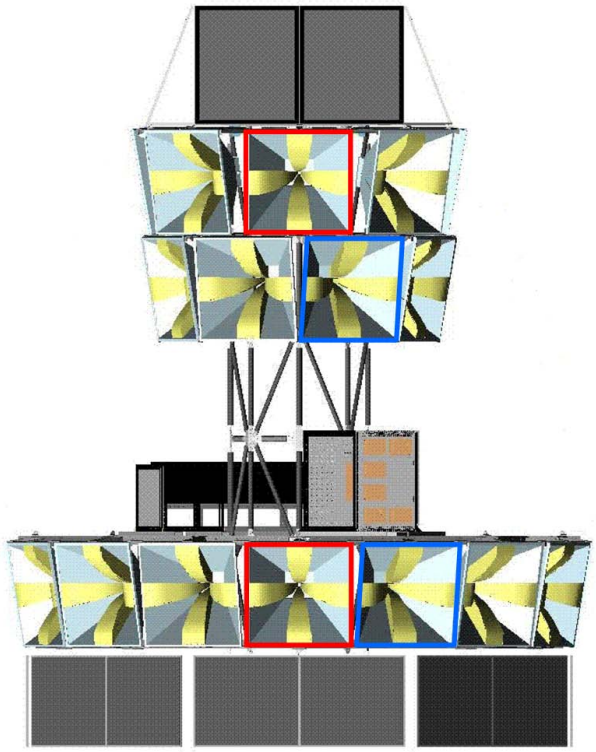

Figure 1: Engineering schematic of the ANITA Instrument [9]. Top and bottom solar panels shown in black. Instrument boxes placed on frame above lower ring of antennas. Adjacent instrument phi sectors are highlighted in red and blue. Not pictures are 4 discone and 4 bicone antennas used in the calibration analysis.

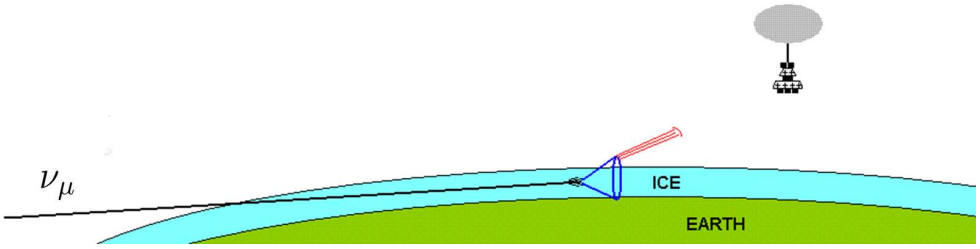

Figure 2: Representation of a neutrino interaction event. Transient neutrino enters ice and interacts producing an electron-photon particle shower. Shower undergoes Askaryan effect and radiates a radio pulse to payload suspended 37 km above the ice surface by a long duration balloon.

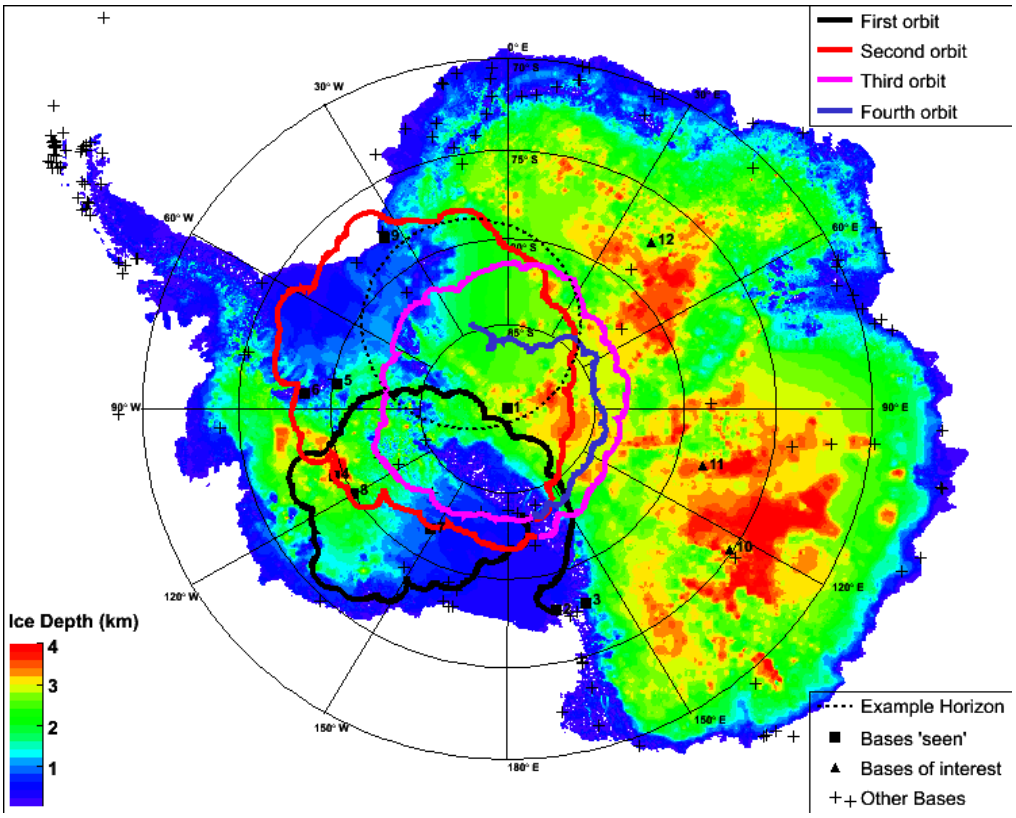

Figure 3: Map of ANITA flight path. Four orbits comprising a total flight time of 35 days. Black dashed line shows an example horizon of radius 600 km [10].

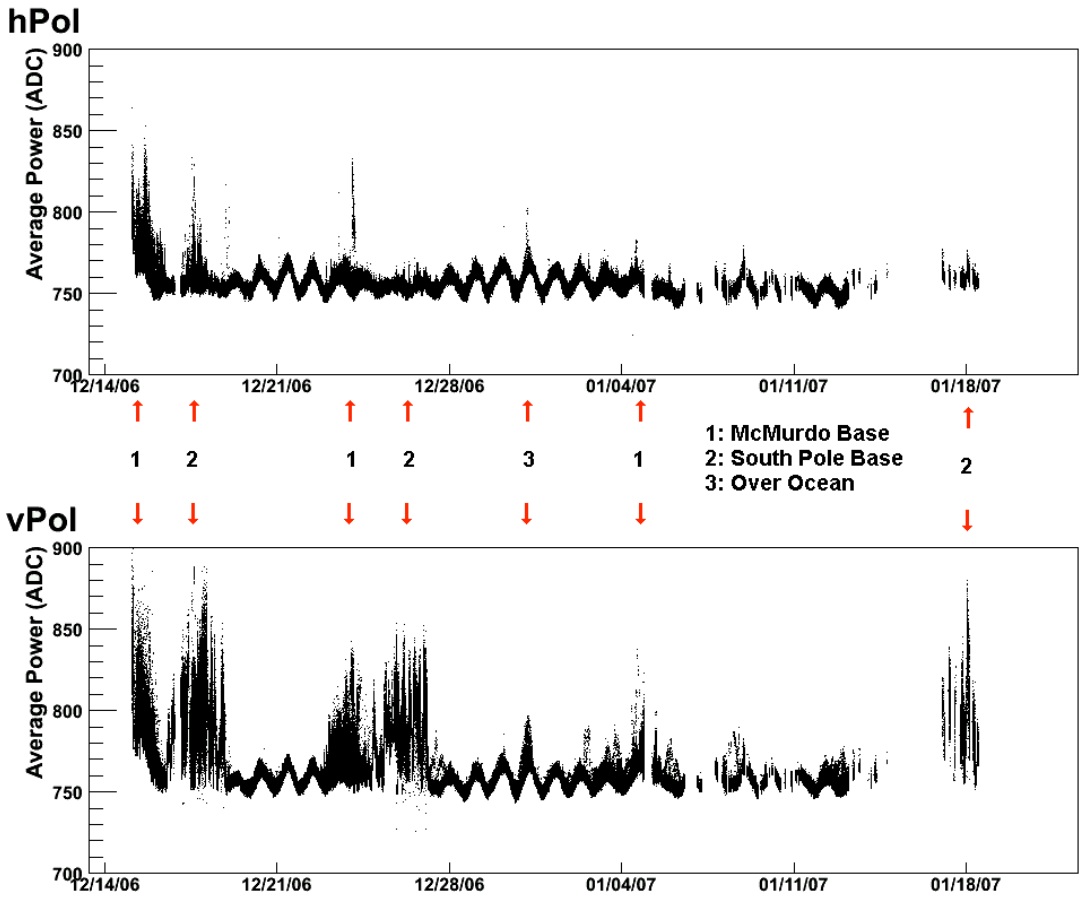

Figure 4: RF background plotted as a function of time. RF Power in ADC counts is averaged for the 32 horizontal channels in the top panel and the 32 vertically polarized channels in the bottom panel. Large spikes in power are labeled by noise source. Sinusoidal variation is due to diurnal cycle, with amplitude dependent on payload latitude. Gaps in data are caused by a computer malfunction that left the instrument off at those times.

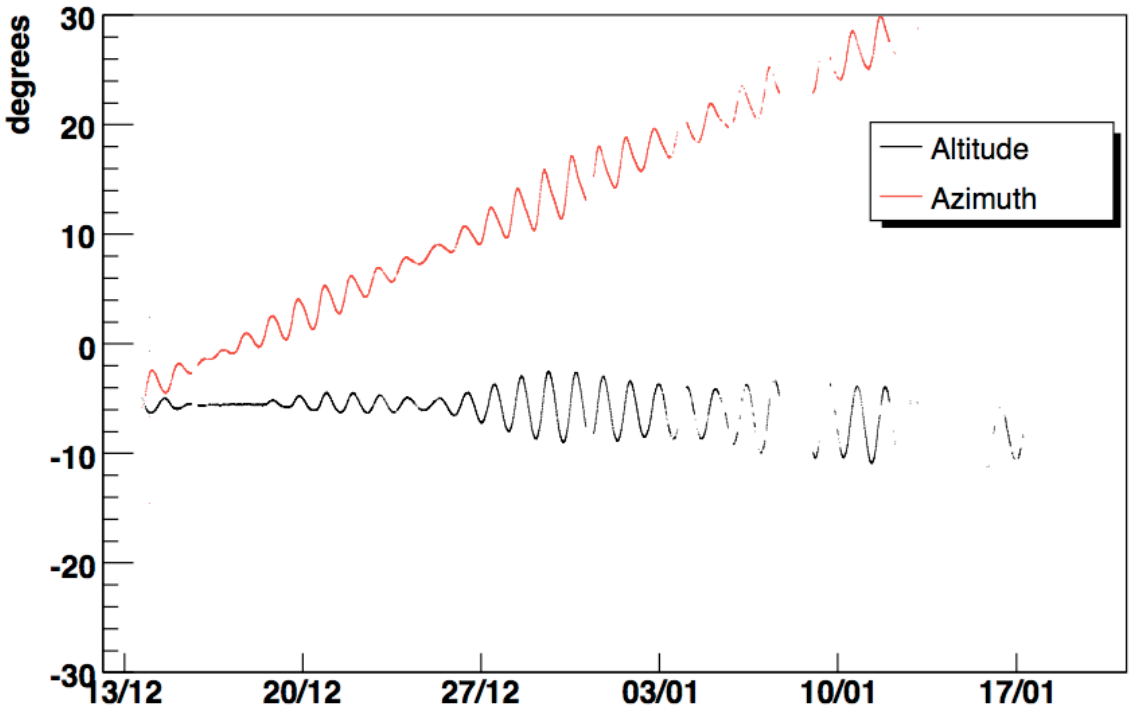

Figure 5: Sun and Galactic Center separation in ANITA alt/az as a function of time with $\Delta\theta$ = sun − galactic center for both altitude and azimuth. Sinusoidal pattern is derived from the amplitude of the diurnal period. This is dependent on the latitude of the payload as seen in the background thermal noise in Fig. 4.

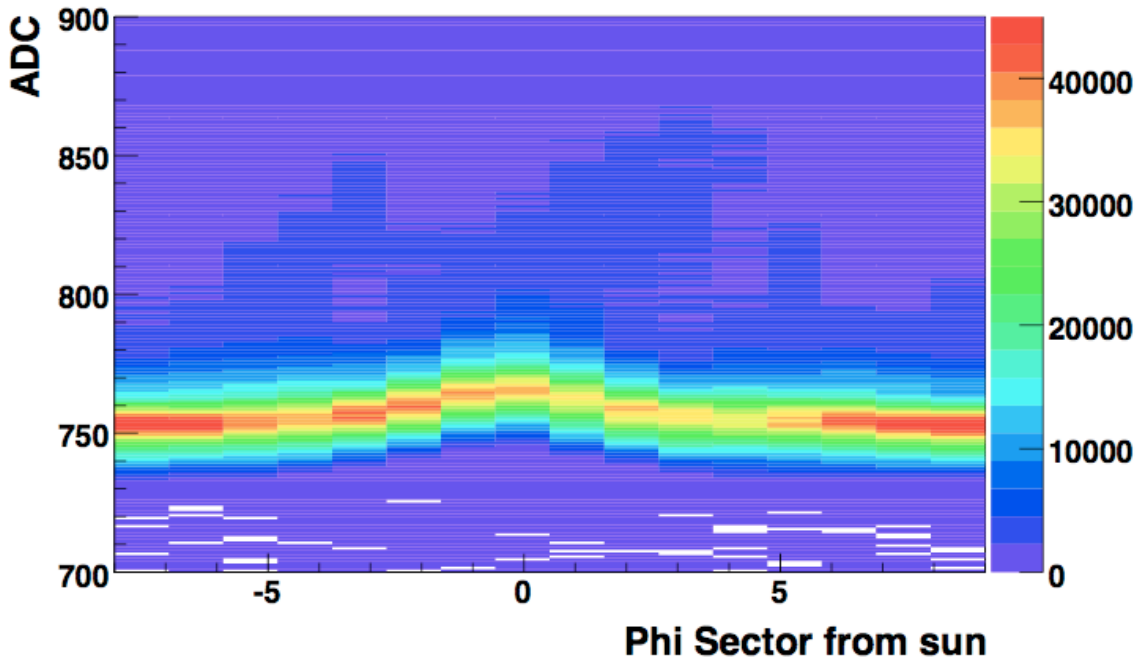

Figure 6: Average power plotted for each phi sector with the sun centered at zero for all times when the payload was within 600 km of the South Pole. Colors represent the number of entries in each bin. Graph shows an excess in the solar direction which is due to a combination of both a solar component and a component form the galactic center.

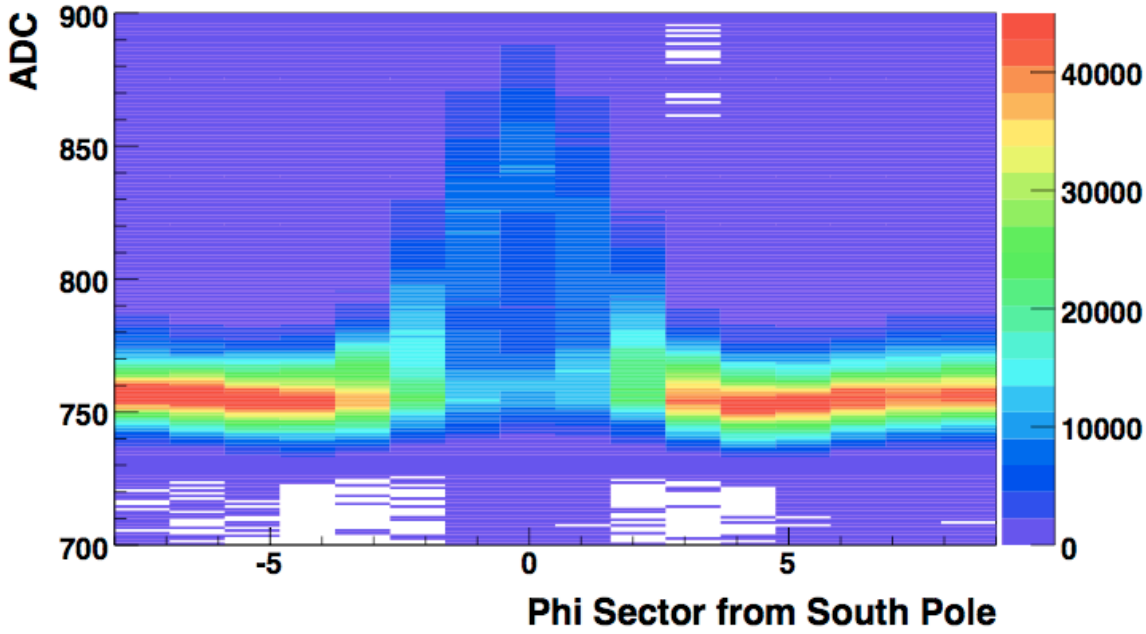

Figure 7: Same data as Fig. 6 plotted with South Pole at 0. Large peak shows South Pole base has a significant noise effect above the thermal background.

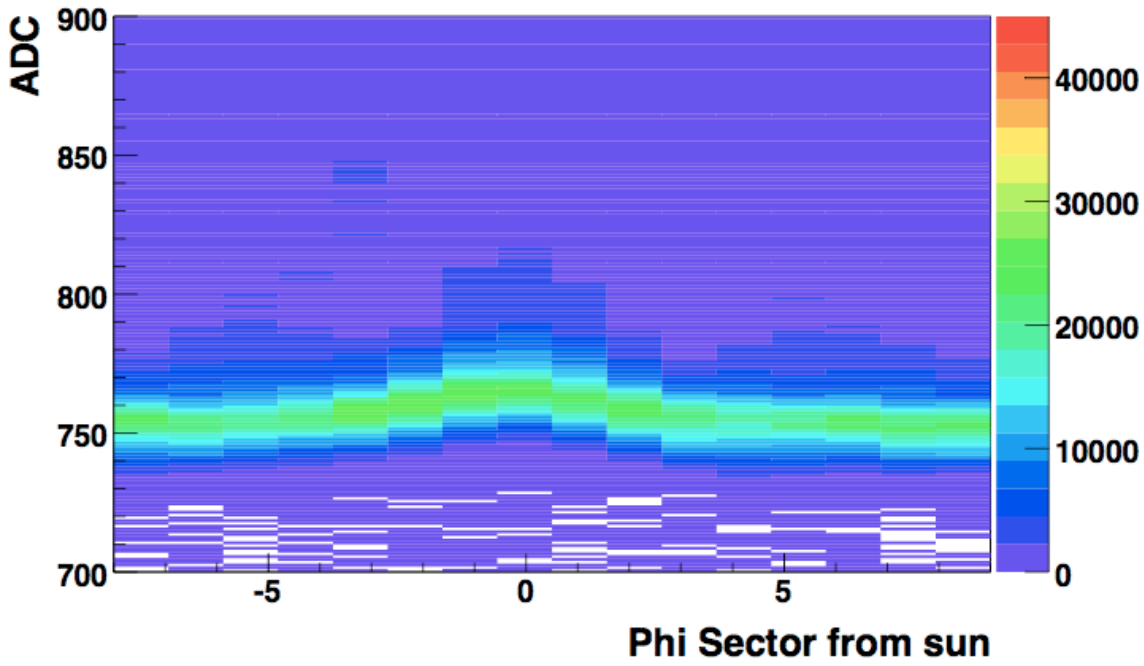

Figure 8: Data from Fig. 6 plotted with phi sectors occupied by the south pole removed. Color scale is kept the same for constant number resolution per bin. Graph shows smoothing effect that removing the south pole has on the power distribution bringing it down to the noise floor.

Table 1: Table of Cuts Used in Cross-Correlation Analysis

Cut	Value	Comment
Antenna Max	Ant14	Antenna with maximum correlation value
Polarization Max	Vertical Polarization	Polarization with maximum correlation value
Maximum	> 5000	Correlation value on Ant14 vPol
Sum of Absolute Value	> 50000	Sum of absolute value of correlation on Ant14 vPol
Delay	< 15ns	Timing delay on Ant14 vPol correlation
Width of NHE	< 10	Width of Normalized Hilbert Envelope (NHE) on Ant 14 vPol

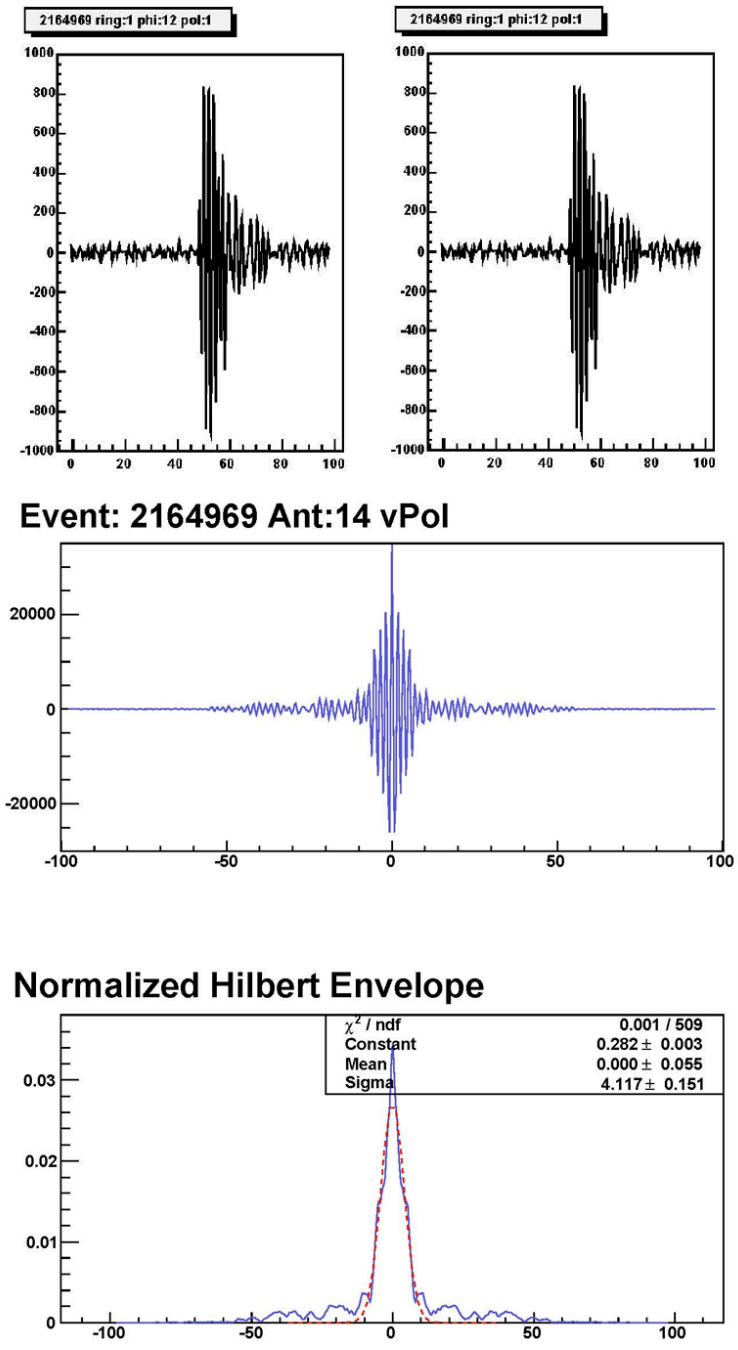

Figure 9: Cross-correlation of waveforms in top panel shown in middle panel. Normalized hilbert envelop fitted with a Gaussian distribution shown in bottom panel. This figure shows the Auto-Correlation on the Antenna 14 Vertical polarization.

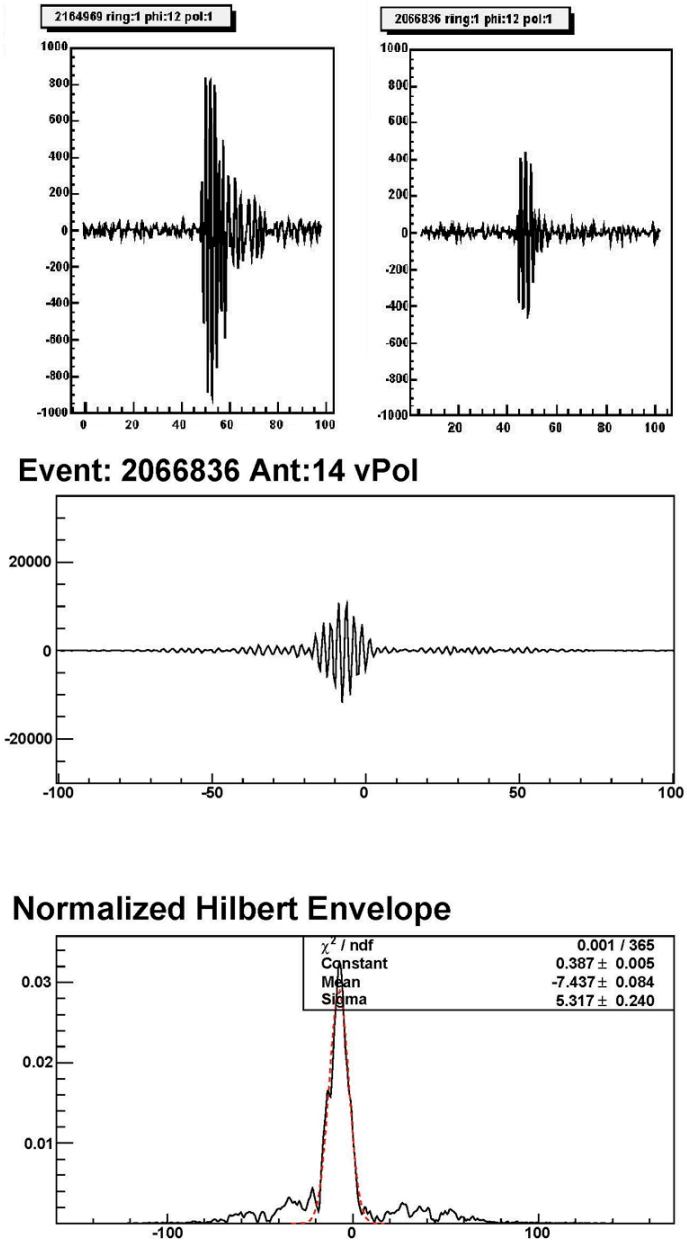

Figure 10: Cross-correlation of waveforms in top panel shown in middle panel. Normalized hilbert envelop fitted with a Gaussian distribution shown in bottom panel. This figure shows an example of a good correlation with the template waveform in Fig. 9 and pulse on Antenna 14 Vertical polarization.

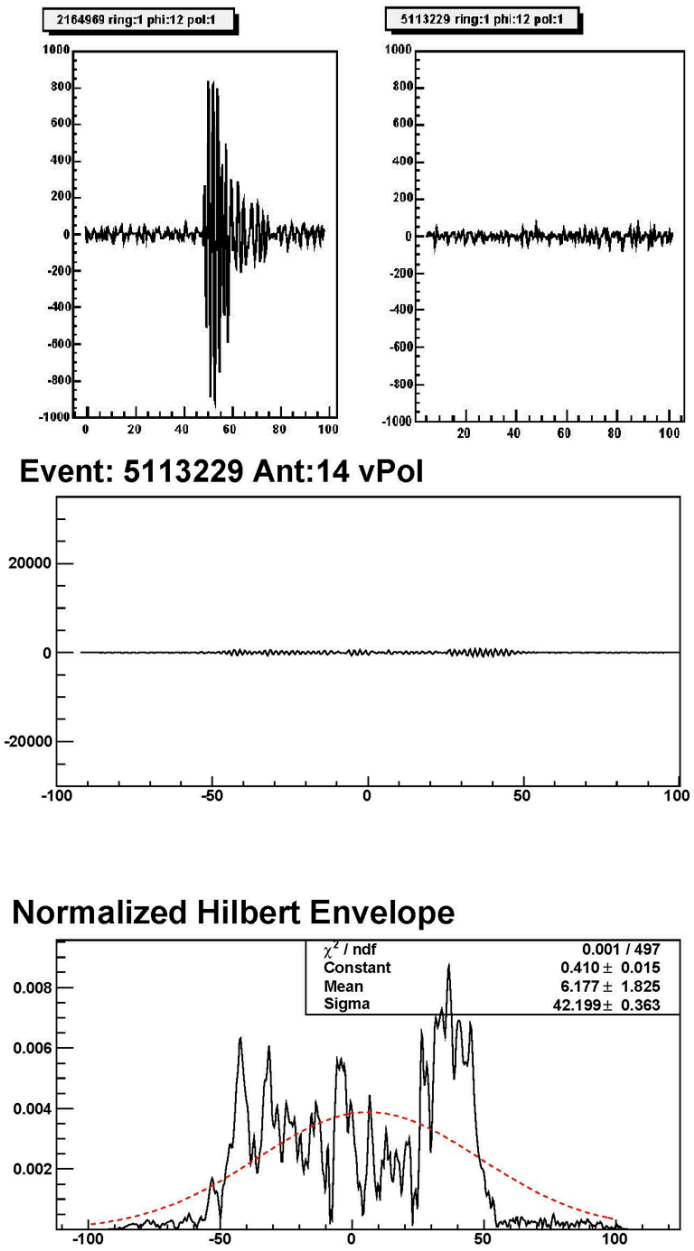

Figure 11: Cross-correlation of waveforms in top panel shown in middle panel. Normalized hilbert envelop fitted with a Gaussian distribution shown in bottom panel. This figure shows an example of a bad correlation with the template waveform in Fig. 9 and a noise event on Antenna 14 Vertical polarization.

Figure 12: Visualization of cross-correlation analysis results. Gray "x" and line show expected pulsing senquence from software labels. Pulsing sequence is 4-3-2-1. Blue triangles show pulses found with cross-correlation analysis. Other symbols are tags for certain classes of pulses that were found.